# Effect of B$_2$O$_3$ and Basic Oxides on Network Structure and Chemical Stability of Borosilicate Glass

**Ming Lian [1], Tian Wang [1],\* and Chong Wei [2,3,4],\***

[1] School of Materials Science and Engineering, Shaanxi University of Science and Technology, Xi'an 710021, China; 13759678619@163.com

[2] Science and Technology on Thermo Structural Composite Materials Laboratory, Northwestern Polytechnical University, Xi'an 710072, China

[3] School of Mechanics, Civil Engineering and Architecture, Northwestern Polytechnical University, Xi'an 710072, China

[4] Research & Development Institute, Northwestern Polytechnical University in Shenzhen, Shenzhen 518057, China

\* Correspondence: wangtian@sust.edu.cn (T.W.); chong.wei@nwpu.edu.cn (C.W.)

**Abstract:** Glass properties play crucial roles in ensuring the safety and reliability of electronic packaging. However, challenges, such as thermal expansion and resistance to acid corrosion, pose long-term service difficulties. This study investigated the impact of the microstructure on acid resistance by adjusting the glass composition. A glass material with excellent acid resistance was obtained by achieving a similar coefficient of thermal expansion to tantalum; it exhibited a weight loss rate of less than 0.03% when submerged in 38% sulfuric acid at 85 °C for 200 h. Theoretically, this glass can be used to seal wet Ta electrolytic capacitors. Differential scanning calorimetry (DSC) was used to analyze the glass transition temperature and thermal stability of borosilicate glasses. X-ray diffractometry (XRD), scanning electron microscopy (SEM), and Raman spectroscopy were used to study the microstructure of the amorphous phase of the borosilicate glass, which revealed a close relationship between the degree of network phase separation in the borosilicate glass and the degree of polymerization (isomorphic polyhedron value, IP) of the glass matrix. The IP value decreased from 3.82 to 1.98 with an increasing degree of phase separation. Boron transitions from [BO$_4$] to [BO$_3$] within the glass network structure with increasing boron oxide content, which diminishes the availability of free oxygen provided by alkaline oxide, resulting in a lower acid resistance. Notably, the glass exhibited optimal acid resistance at boron trioxide and mixed alkaline oxide contents of 15% and 6%, respectively. Raman experiments revealed how the distributions of various bridging oxygen atoms (Q$_n$) affect the structural phase separation of the glass network. Additionally, Raman spectroscopy revealed the depolymerization of Q$_4$ into Q$_3$, thereby promoting high-temperature phase separation and highlighting the unique advantages of Raman spectroscopy for phase recognition.

**Keywords:** tantalum capacitor; borosilicate; TiO$_2$; B$_2$O$_3$; sealing; Raman

## 1. Introduction

Liquid tantalum electrolytic capacitors have a large capacitance, are not easy to break down, have low internal resistance and are small in size, and their demand has been increasing [1,2]. However, it contains extremely corrosive gel sulfuric acid inside. If the seal is not good, it will leak out from the inside, which will corrode the surrounding electronic components and cause adverse effects on the entire electrical appliance. Therefore, liquid electrolyte tantalum capacitors require strict hermetic sealing with glass. The current research on sealing glass is mainly aimed at the flat solid oxide fuel cell, and there is little research on the sealing glass with a low expansion coefficient for tantalum capacitors [3]. In addition, the existing electronic component sealing glass contains a large amount of metal

lead. For example, the lead content of the existing electronic sealing glass brand DB-435 is 34%, and the lead content of DH-704 is 77%. The heavy metal lead is not only harmful to the human body but also does not meet the requirements of environmental protection. Therefore, a kind of non-toxic and harmless sealing glass which can be used for the sealing of liquid tantalum electrolytic capacitors is very important. Therefore, it is desirable for the glass to approach the low thermal expansion coefficient of tantalum ($\alpha = 5.7 \times 10^{-6}$ K$^{-1}$) at 300 °C (the operating temperature of tantalum electrolytic capacitors).

Due to the large difference between the thermal expansion coefficients of metal and glass, a large thermal stress will be generated inside the glass sealed with metal at a high temperature, resulting in glass and metal materials that cannot be directly sealed. The main difficulty of tantalum metal sealing technology is to produce glass materials with similar thermal expansion coefficients to achieve matching sealing between glass and tantalum metal materials. The larger the thermal expansion coefficient of the sealing glass material, the lower its stability and thermal shock resistance [4–7]. Therefore, a good sealing glass needs to have a thermal expansion coefficient similar to that of metal and at the same time, ensure excellent stability and strength [8,9]. The composition of the sealing glass directly affects its own thermal expansion performance, operability, chemical stability, and mechanical strength and also affects the tightness of its sealing with metal materials. So the composition of transition glass is very important [10].

Borosilicate glass has good heat resistance, good chemical stability and mechanical properties, and is widely used in the fields of heat resistance, pharmaceutics, aviation, packaging glass, and electrical glass [11,12]. Low-expansion borosilicate glass has become a hot spot in the field of glass research in recent years. With the development of science and technology, the application field and market prospect of borosilicate glass are also expanding. The structure of borosilicate glass is different from that of ordinary soda–lime–silica glass. In this glass system, alkali metal oxides provide free oxygen to convert the boron–oxygen trihedron [BO$_3$] into a boron–oxygen tetrahedron [BO$_4$]. The structure is transferred from layer to shelf; [BO$_4$] can be used as a network former to connect with the silicon–oxygen tetrahedron [SiO$_4$], increasing the integrity and tightness of the glass, so the glass performance of this system is excellent. However, low-expansion borosilicate glass faces the problems of a high melting point, high viscosity, and easy separation in the preparation process. Wan et al. studied the effect of [BO$_4$] on the thermal expansion and phase separation of borosilicate glass. The results showed that there was no obvious improvement in the phase separation of the glass [13,14], and the expansion coefficient increased with the increase in Al$_2$O$_3$ content. Liu Guanglong et al. found that the addition of Al$_2$O$_3$ can increase the high temperature surface tension of borosilicate glass and increase its viscosity at 1530 °C. He Feng et al. found that adding B$_2$O$_3$ can improve the chemical stability of glass to a certain extent [15]. This topic will conduct research on sealing glass with a lower expansion coefficient for sealing tantalum capacitors and analyze its performance.

Therefore, in this study, the transition temperature and thermal stability of borosilicate glasses were studied by differential scanning calorimetry (DSC). The effects of basic oxides and B$_2$O$_3$ on the thermal expansion and microstructure of the glass matrix were studied by X-ray diffraction (XRD) and scanning electron microscopy (SEM) and thermal expansion analysis. The effects of the ratio of [BO$_3$] and [BO$_4$] in the basic glass network structure on the degree of polymerization, isomorphic polyhedron polymerization index (IP) value of the glass network and the acid resistance of the glass were studied by Raman spectroscopy and the weight loss method.

## 2. Materials and Methods

### 2.1. Material Preparation

The low-expansion borosilicate glass composition prepared in this study was composed of SiO$_2$, B$_2$O$_3$, Al$_2$O$_3$, BaO, K$_2$O, Na$_2$O, Fe$_2$O$_3$, TiO$_2$, ZrO, Li$_2$O, and the high-entropy oxide powder (LaCePrZr)O$_2$, custom-tailored by the Ultra-High Temperature Laboratory at Northwestern Polytechnic University. The uniform mixture of raw materials was

melted at 1500 °C for 3 h to prepare borosilicate glass with varying $B_2O_3$ and alkaline oxide contents. The nominal composition of the glass, expressed in wt%, is listed in Table 1.

**Table 1.** Composition of samples in this work.

| Composition (wt %) | Example | | | | | |
|---|---|---|---|---|---|---|
| | $A_1$ | $A_2$ | $A_3$ | $A_4$ | $A_5$ | $A_6$ |
| $SiO_2$ | 59.7 | 58.7 | 58.2 | 55.2 | 55.7 | 56.7 |
| $B_2O_3$ | 12 | 12 | 12 | 15 | 15 | 15 |
| $Al_2O_3$ | 7 | 7 | 7 | 7 | 7 | 7 |
| BaO | 6 | 6 | 6 | 6 | 6 | 6 |
| $K_2O$ | 5 | 4 | 5.5 | 4 | 5 | 3 |
| $Na_2O$ | 3 | 5 | 4 | 5.5 | 4 | 5 |
| $Fe_2O_3$ | 0.3 | 0.3 | 0.3 | 0.3 | 0.3 | 0.3 |
| $TiO_2$ | 3 | 3 | 3 | 3 | 3 | 3 |
| ZrO | 2 | 2 | 2 | 2 | 2 | 2 |
| $Li_2O$ | 1 | 1 | 1 | 1 | 1 | 1 |
| High-entropy oxide | 1 | 1 | 1 | 1 | 1 | 1 |
| Linear expansion coefficient ($10^{-7}$ °C$^{-1}$) | 7.9 | 7.8 | 6.9 | 5.8 | 5.7 | 5.5 |
| Softening temperature (°C) | 570 °C | 574 °C | 569 °C | 570 °C | 609 °C | 630 °C |

The addition of alkali metal oxides, such as sodium oxide, barium oxide, and potassium oxide, can increase the characteristic temperature of glass. Among these, potassium oxide and sodium oxide specifically reduce the coefficient of thermal expansion (CTE) and increase the phase transition temperature. In contrast, barium oxide, which has a high expansion coefficient, significantly influences the glass expansion coefficient. The boron oxide content varied within the 10–15% range, and a comparative test was used to identify a glass formulation with an expansion coefficient close to that of tantalum metal.

To enhance the acid resistance of the glass, a certain amount of $TiO_2$ was introduced into the basic glass composition. This study aimed to identify a glass formulation that exhibited superior acid resistance. The addition of an appropriate amount of $TiO_2$ was found to benefit a more stable glass network structure, thereby enhancing the stability of the borosilicate glass structure and leading to significantly improved acid corrosion resistance. Titanium (Ti) is typically positioned within the octahedra of a borosilicate glass system and serves as an external component of the glass network; however, it is positioned within tetrahedra and becomes part of the network at high alkali metal contents. The $TiO_2$ nucleating agent plays a prominent role in densifying the glass network structure and substantially enhances acid resistance [16,17].

The potassium oxide content significantly impacts the electrical-insulating properties of both glass and tantalum, with alkali metal oxides tending to degrade the electrical-insulating properties of glass. However, low-alkali borosilicate glass demonstrates superior electrical-insulating properties compared to glass with a high alkali oxide content [18]. An experimental plan was devised to identify borosilicate glass with optimal insulating properties, which involved varying the $K_2O$ content within the 2–4.5 wt % range, with the total alkali metal oxide content ($K_2O$ + $Na_2O$) maintained at 8–9.5 wt %.

Our experiments were conducted effectively by employing a three-factor three-level orthogonal design that generated nine sets of experiments based on the aforementioned variables. Among these, three sets of borosilicate glass exhibited excessively high surface tensions at 1500 °C, rendering them unsuitable for casting. Consequently, we selected six sets ($A_1$–$A_6$) for use in the orthogonal experiments, as presented in Table 1. The addition of high-entropy oxide powders (($LaCePrZr)O_2$) with negative thermal expansion coefficients is aimed at further adjusting the coefficient of thermal expansion (CTE) of borosilicate glass, with the expectation of obtaining borosilicate glass with a lower CTE.

The mixture was prepared by combining the raw materials with absolute ethanol at a 2.6:1 ($w/w$) absolute ethanol–mixture ratio. Ball milling was performed using an $Al_2O_3$ ball

mill with a raw-material-to-$Al_2O_3$-ball-mill volume ratio of 1:2. Appropriately adjusting the proportion of the ball mill stones ensures that the raw materials are uniformly mixed, minimizes material wastage, and reduces the formation of bubbles and nonuniformity during high-temperature melting. Ball milling was performed for 130–180 min at 300–350 r/min. After ball milling for 4 h, the slurry was transferred to a drying oven and dried at 40 °C.

Multistage heating was used to facilitate better control of each stage of the molten-glass heating process during high-temperature sintering. The following specific operating parameters were used: The temperature was first raised to 900 °C at 5–10 °C/min and held there for 2 h. The temperature was then further raised to 1500 °C at 5 °C/min and maintained there for 3 h.

The material was incubated at 900 °C for 2 h and held at 1500 °C for 3 h in a muffle furnace to completely melt the raw materials and eliminate bubbles. The resulting clear glass liquid was poured into a graphite mold, cooled, and demolded. The glass was subsequently annealed by placing it in a preheated muffle furnace at 580 °C for 3 h. The annealed glass was cut into small pieces 10 × 10 × 1.5 mm in size using a low-speed diamond saw. These pieces were ground and polished to obtain brown borosilicate hard glass.

Formulations $A_1$–$A_6$ were selected to have preferred raw material mass percentage ranges. The properties of the resulting glass were evaluated using 5 mm diameter cylindrical samples prepared from the sealing glass that were approximately 25 mm high. These samples were then subjected to high-temperature horizontal dilatometry to measure the thermal expansion coefficient $\alpha$. The thermal expansion coefficients of glasses formulated with each raw material component are presented in Table 1. Furthermore, acid resistance testing was conducted using the weight loss method, in which the sealed glass is cut into small pieces 10 × 10 × 10 mm in size and immersed in 38% sulfuric acid at 85 °C for 200 h. The weight loss rate of the glass was determined.

## 2.2. Differential Thermal Analysis (DTA)

The thermal behavior of the powdered glass samples was examined using a differential thermal analyzer (DTA, SDTQ 600–TA Chiyoda, Tokyo, Japan) to determine the glass $T_g$ temperature (glass transition temperature) and Tc temperature (crystallization temperature), and the ground glass powder was put into the special dry crucible for the test; the test temperature range is 0–1300 °C, the heating rate is 10 °C $min^{-1}$, and $Al_2O_3$ is used as the reference in a high-purity nitrogen environment.

## 2.3. X-ray Diffraction Analysis (XRD)

The crystalline phase is determined by X-ray diffraction (XRD, X'pert Pro-Powder, PANalytical Dan Dong, Liao Ning Province, China) using Cu K$\alpha$ radiation with a wavelength of 0.154 nm, in the 2-theta/° range from 10° to 80°, and a scan speed of 5°/min of the scanning rate at room temperature, which is operated at 40 KV and 40 mA. The XRD data are subjected to fit profile processing using X'Pert High Score Plus(9.0).

## 2.4. Scanning Electron Microscope (SEM)

The microstructure characterization of the crystallized specimens was carried out using a scanning electron microscope equipped with an energy-dispersive spectrometer (SEM/EDS, Quanta FEG 250, Chiyoda, Tokyo, Japan). For SEM characterization, freshly fractured surfaces' crystallized specimens were etched by immersion in a (4% HF) solution for 1 min. After that, the samples were washed with distilled water and dried in the dryer at 120 °C for 1 h. The fracture surfaces were coated with electro-conductive gold film for good conductivity by the sputtering method.

## 2.5. Thermal Expansion Coefficient

The thermal expansion coefficient (TEC) of the glass-ceramic materials was measured linearly from the thermal expansion curve and was determined using a contact dilatometer,

a thermal mechanical analyzer (Model: DIL-407PC, Netzsch, Linseis Germany), at a heating rate of 10 °C/min in the temperature range between 25 and 800 °C. The average linear TEC of the bulk glass-ceramic rods of dimensions 25 mm × 5 mm were calculated using the following equation:

$$\alpha = \frac{\Delta L}{L_0 \Delta T}$$ (1)

where $\Delta L$, $L_0$, and $\Delta T$ are the linear expansion, the initial length of the sample, and the specified temperature interval, respectively.

### 2.6. Raman Spectroscopy

Raman spectroscopy was performed at room temperature using a Renishaw inVia spectrometer and a Peltier-cooled CCD detector(United Kingdom-London Renishaw). The solid-state laser operated at a wavelength of 532 nm with a spot diameter of about 2–3 μm. The laser beam was focused onto a microscope to collect the scattered light. A laser power of less than 1 mW was selected to optimize the signal-to-noise ratio and avoid thermal effects. Each Raman spectrum was acquired for 60 s in order to obtain a fine resolution of less than 1 cm$^{-1}$, and the collected Raman spectra were matched against standard Raman spectra in the RRUFF database. The data were optimized by adjusting the baseline and smoothing minima, and the acquired data were fitted using Igor software (9.0) to provide data references for subsequent research. Igor software is easily used to process Raman spectroscopy data; it efficiently processes substrates and performs multipeak fitting simultaneously.

## 3. An Analysis of the Intrinsic and Corrosion Resistance Properties of Glass

### 3.1. Dynamics and Microstructure Analysis

Glass formulations $A_1$–$A_6$, prepared using an orthogonal experimental process, were finely ground to obtain glass powders. Each powder was carefully placed in a test mold and subjected to XRD at 2θ values in the 10–80° range. The XRD patterns displayed in Figure 1 reveal a lack of crystallization peaks, consistent with a complete and high-quality glass network structure. Additionally, Raman spectroscopy was used to further analyze the glass phase network structure in subsequent stages.
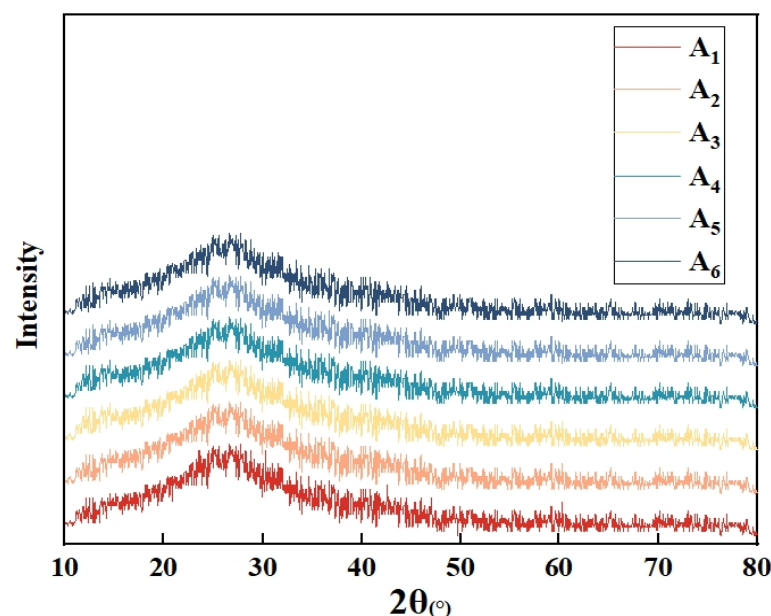


**Figure 1.** XRD pattern of base glass.

Borosilicate glasses with various compositions were subjected to differential thermal analysis (DTA), and their thermal expansion coefficients (CTEs) were determined. Specific glass transition temperatures ($T_x$) are listed in Table 2, which reveals that Tx is positively correlated with the alkaline oxide content. Thermal expansion coefficients are shown as functions of temperature in Figure 2a; Figure 2b shows the thermal expansion curves of the samples, from which it can be seen that the expansion coefficients of $A_1$–$A_3$ are significantly lower than those of $A_5$–$A_6$. The coefficients of thermal expansion of the samples at 300 °C were calculated and are presented in Table 1. There is a positive correlation with the silica content.

**Table 2.** Raman peak area and Ip value of base glass.

|  | $A_1$ | $A_2$ | $A_3$ | $A_4$ | $A_5$ | $A_6$ |
|---|---|---|---|---|---|---|
| $Q_1$ Peak position | 781 cm$^{-1}$ | 765 cm$^{-1}$ | 782 cm$^{-1}$ | 780 cm$^{-1}$ | 759 cm$^{-1}$ | 784 cm$^{-1}$ |
| $Q_2$ Peak position | 920 cm$^{-1}$ | 904 cm$^{-1}$ | 880 cm$^{-1}$ | 880 cm$^{-1}$ | 894 cm$^{-1}$ | 887 cm$^{-1}$ |
| $Q_3$ Peak position | 1012 cm$^{-1}$ | 990 cm$^{-1}$ | 981 cm$^{-1}$ | 1025 cm$^{-1}$ | 1011 cm$^{-1}$ | 970 cm$^{-1}$ |
| $Q_4$ Peak position | 1090 cm$^{-1}$ | 1069 cm$^{-1}$ | 1036 cm$^{-1}$ | 1136 cm$^{-1}$ | 1121 cm$^{-1}$ | 1090 cm$^{-1}$ |
| $AQ_1$ | 13.14% | 18.54% | 15.58% | 10.65% | 13.24% | 17.55% |
| $AQ_2$ | 13.05% | 10.88% | 11.07% | 21.67% | 16.01% | 14.06% |
| $AQ_3$ | 13.58% | 23.06% | 39.68% | 42.70% | 55.49% | 59.53% |
| $AQ_4$ | 60.22% | 47.50% | 33.65% | 24.97% | 15.25% | 8.84% |
| $A_{500}$ | $3.09 \times 10^6$ | $3.05 \times 10^6$ | $2.70 \times 10^6$ | $3.66 \times 10^6$ | $2.98 \times 10^6$ | $2.61 \times 10^6$ |
| $A_{1000}$ | $8.10 \times 10^5$ | $8.62 \times 10^5$ | $1.19 \times 10^6$ | $1.42 \times 10^6$ | $1.18 \times 10^6$ | $1.32 \times 10^6$ |
| Ip | 3.82 | 3.51 | 2.58 | 2.26 | 2.21 | 1.98 |
| NBO/(NBO + BO) | 0.21 | 0.27 | 0.29 | 0.33 | 0.34 | 0.37 |
| Tg | 538 | 544 | 536 | 530 | 553 | 537 |
| Tx | 507 | 521 | 516 | 551 | 549 | 557 |
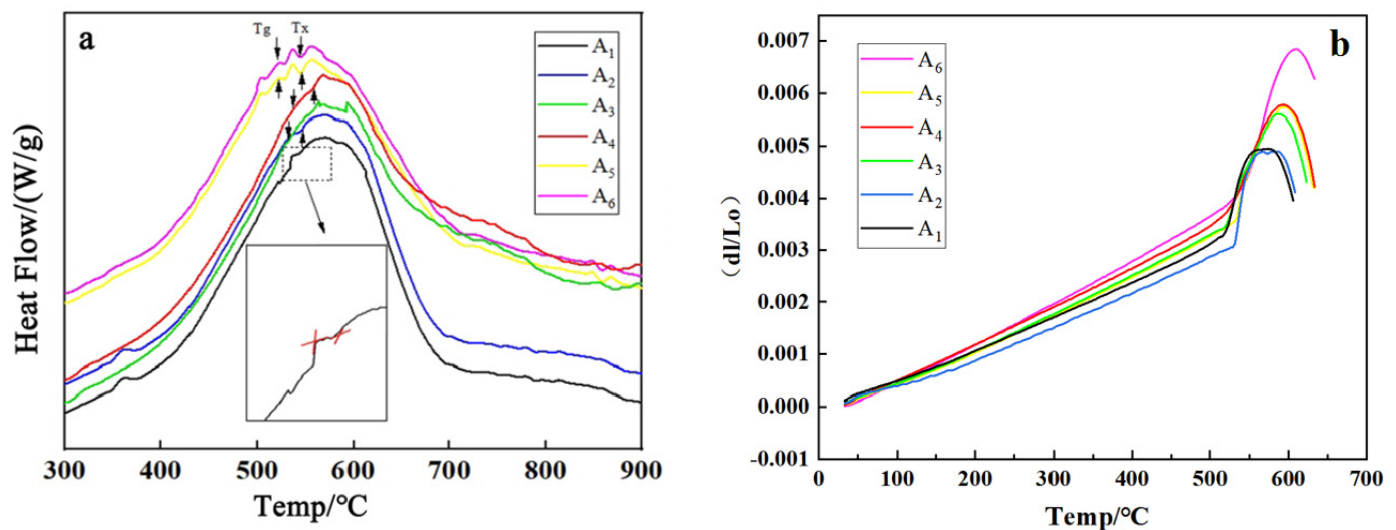


**Figure 2.** Glass transition temperature (**a**) and thermal expansion coefficient (**b**) of base glass.

Figures 3–7 show the thermal expansion curves for each of the six groups of borosilicate glasses in the RT-700 °C interval. It can be seen that the CTE curve changes from a flat to a sudden rise between 500 and 600 °C, which is due to the transition from the glassy state to the highly elastic state that occurs in this interval. The corresponding characteristic temperature is the glass transition temperature Tx, which is basically consistent with the 500–600 °C obtained from the DSC curve.
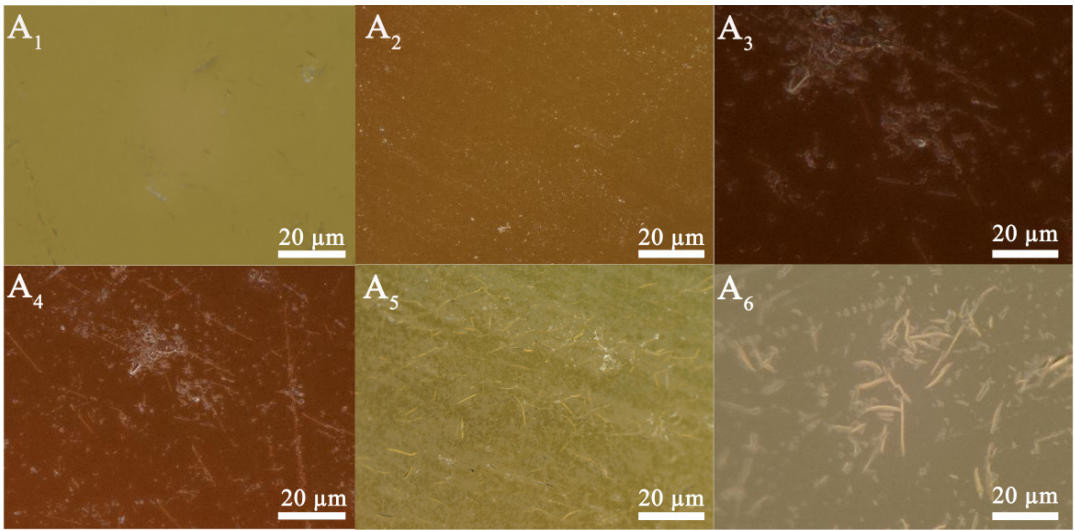
**Figure 3.** Micromorphologies of samples under light microscope after 4% HF solution etching for 60 s (($A_1$–$A_6$) in order).
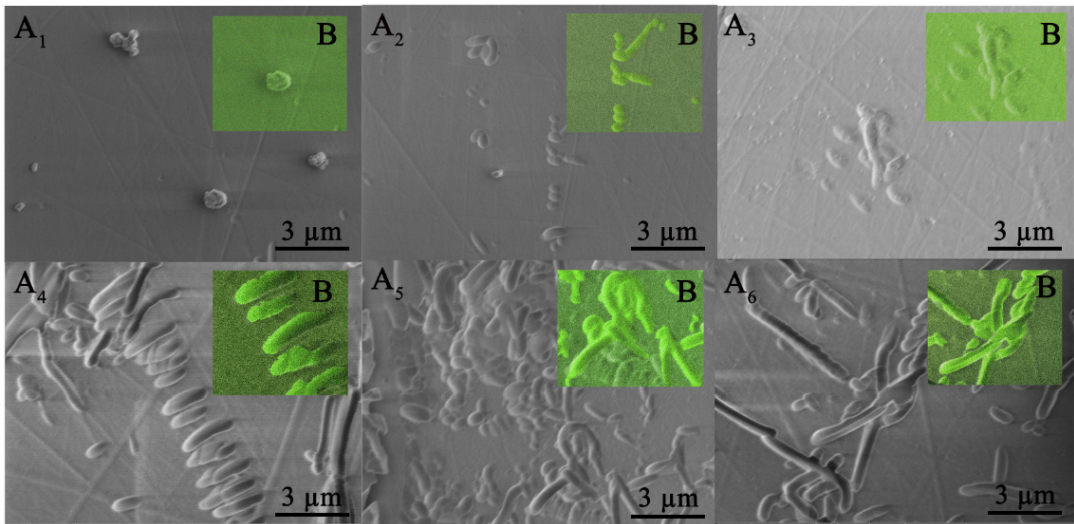


**Figure 4.** SEM and EDS of borosilicate glass after 60 s by 4% HF etching solution (green area represents B element EDS).
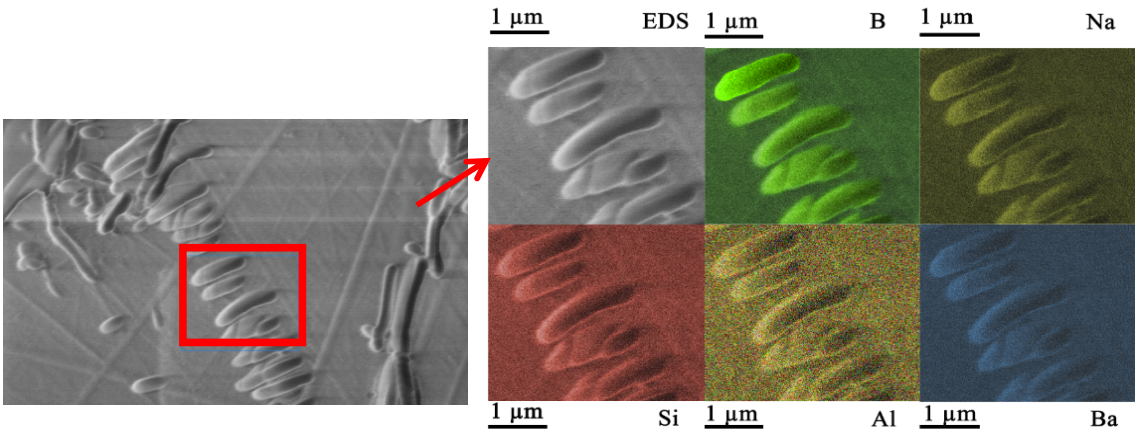


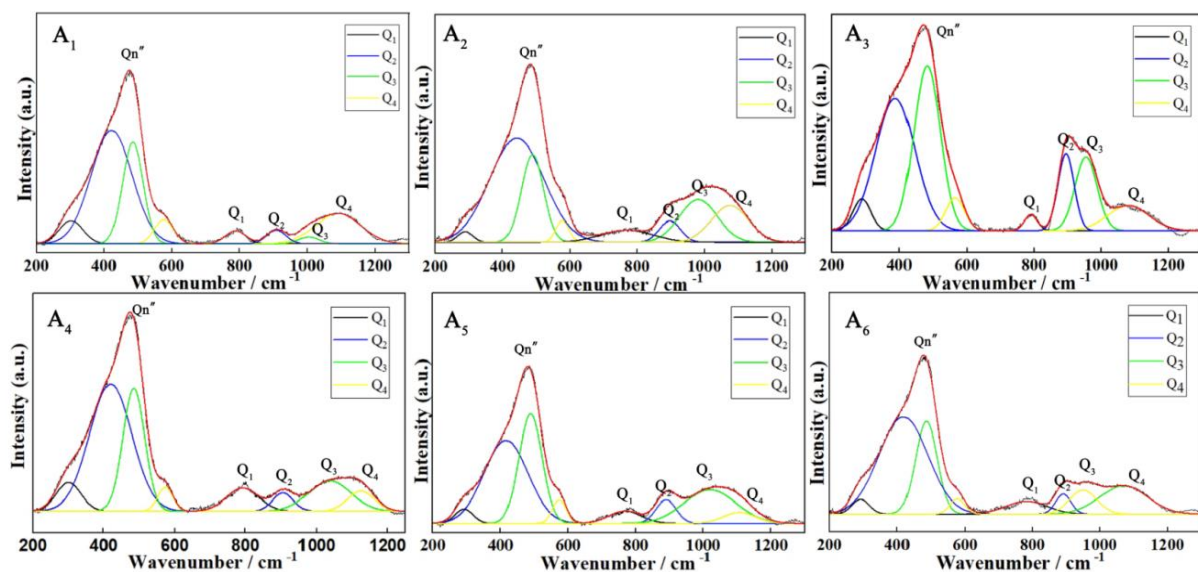**Figure 5.** EDS of glass dendritic phase separation.

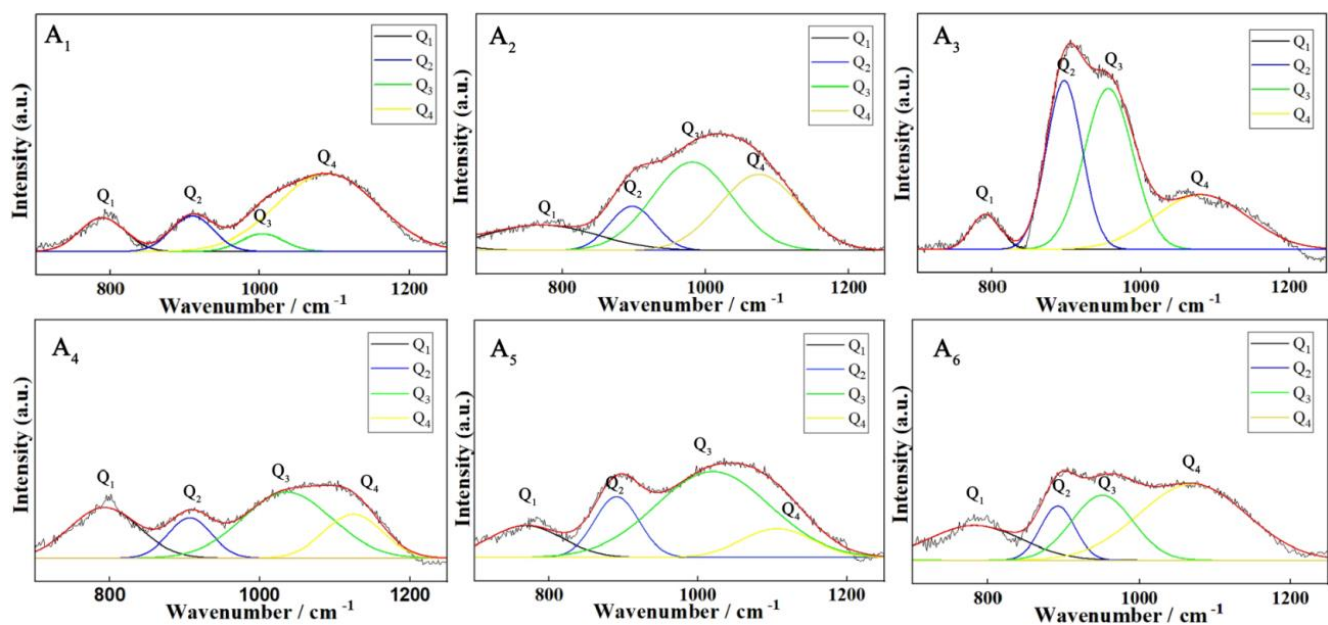**Figure 6.** Raman spectrum of base glass after peak fitting.



**Figure 7.** The Raman spectra of the stretching vibration (700 $cm^{-1}$–1200 $cm^{-1}$) of borosilicate glass ($A_1$–$A_6$).

After polishing, six groups of samples were corroded in 4% HF solution for 60 s, and the corroded samples were observed by an optical microscope and scanning electron microscope in Figures 3 and 4, respectively. The sample showed an obvious interconnected phase after corrosion. As can be seen from the EDS diagram in Figure 5, the phase separation degree gradually increases when moving from $A_1$ to $A_6$, forming a boron-rich phase in the dendritic phase separation region.

A lower $B_2O_3$ content was found to correspond to a higher proportion of non-bridging oxygen atoms in the glass network structure. The bridging oxygen content is closely related to the $SiO_2$ and basic oxide contents. Boron exists in the form of $[BO_4]$ and connects silicon–oxygen tetrahedra through bridging oxygen atoms (Si-O-B) in the network structure in glass with a low $B_2O_3$ content, provided that there is sufficient free oxygen in the glass. However, the supply of free oxygen from the basic metal oxide is insufficient at high $B_2O_3$

contents, which limits the ability of boron to form boron–oxygen tetrahedra, resulting in a higher proportion of non-bridging oxygens that undermine the strength of the glass structure. Furthermore, scanning electron microscopy revealed that the phase-separated region in each sample exhibits minor variations in the distributions of other elements, while elemental boron was clearly enriched in one phase, as confirmed by Raman spectroscopy.

The number and positions of the characteristic vibrational peaks in the Raman spectra of the samples did not change as the $B_2O_3$ content increased. According to the relevant literature, the peaks at 398 and 503 cm$^{-1}$ correspond to the bending vibrations of glass bridging oxygens ($Na_2O$-$B_2O_3$-$SiO_2$) and low-expansion glass contains a large amount of $SiO_2$ [18]; hence, the former peak is ascribable to Si-O-Si bending vibrations. The intensities of the bending vibration peaks are very similar between samples, with the peak at 398 cm$^{-1}$ being more intense in each case, consistent with the abundance of Si-O-Si in the structure of each glass. The vibrational peak near 503 cm$^{-1}$ corresponds to the bending vibration of B-O-B in [$BO_4$].

Figure 6 shows Raman spectra of base glasses with varying compositions, which were used to characterize glass network modifications. The Raman spectra reveal two significant regions within the 200–1300 cm$^{-1}$ range, namely one corresponding to the prominent bending envelope of the Si-O bond at 500 cm$^{-1}$ ($A_{500}$) and the other a Qn shoulder band at 1000 cm$^{-1}$ ($A_{1000}$). Here, Qn refers to different bridged oxygen atoms in the glass network (denoted by n). The percentage area of the Raman band obtained through deconvolution and fitting is presented as AQn%. The significance of aggregation was quantified by calculating the aggregation index ($I_P$) as follows [19–21]:

$$Ip = \frac{A_{500}}{A_{1000}} \tag{2}$$

The Ip value is an important parameter that determines the Raman shift of Qn. When the IP values are similar, the degree of glass aggregation can be considered similar. As shown in Table 2, Ip ranges between 2.26 and 2.58 (i.e., it belongs to a group). In addition, base glass samples with different compositions were tested under the same conditions, which revealed that the Qn Raman shift of each sample adopts the following uniform standard: the band at 780 cm$^{-1}$ is attributable to $Q_1$ (three non-bridging oxygens in the tetrahedron), the band at 900 cm$^{-1}$ is assigned to $Q_2$ (two non-bridging oxygens in each tetrahedron), and that at 990 cm$^{-1}$ is due to $Q_3$ (Si–O stretching vibration in each tetrahedron involving a non-bridging oxygen), while the band at 1060 cm$^{-1}$ corresponds to $Q_4$ (Si–O stretching vibration in a fully polymerized unit) [21,22]. The detailed parameters of the glass are listed in Table 2, where AQn is the area occupied by the different fits. Therefore, the ratios of the envelope areas of the four envelope components $Q_1$, $Q_2$, $Q_3$, and $Q_4$ of the tensile vibration peaks at 1000 cm$^{-1}$ of the Raman spectrum of the glass phase to the total area of the tensile vibration ($A_{1000} = AQ_1 + AQ_2 + AQ_3 + AQ_4$) were calculated respectively, and these were denoted as $AQ_1/A_{1000}$, $AQ_2/A_{1000}$, $AQ_3/A_{1000}$, and $AQ_4/A_{1000}$ in order to precisely determine the variations in the glass for each component glass of the glass phase. The IP values were calculated from $A_{500}$ and $A_{1000}$ to represent the degree of polymerization of the glass; Tg is the characteristic temperature of the glass derived from the DTA curve, and Tx is the glass transition temperature of the sample glass.

In order to characterize the modification of the glass network, a multimodal Gaussian fitting approach was employed. The resulting fitting curve of the Raman spectrum within the range of 700–1200 cm$^{-1}$ is presented in Figure 7. By applying the following formula, we can determine the fraction of non-bridging oxygen (NBO/NBO + BO) [23], the average number of NBOs per tetrahedron (NBO/tetrahedron), and the average number of bridging angles per tetrahedron (bridge/tetrahedron):

$$\frac{NBO}{NBO + BO} = \frac{\sum Q^n(4 - n)}{\sum O} \tag{3}$$

### 3.2. Analysis of Acid Resistance Performance

Base glass groups $A_1$–$A_6$ were subjected to acid resistance testing, which revealed the weight loss trends shown in Figure 8 (right). Notably, samples $A_1$–$A_3$ exhibited superior corrosion resistances compared to the $A_4$–$A_6$ samples, with gradual increases in the weight loss rate that correspond to a gradual deterioration in the acid resistance of the base glass observed. SEM images acquired under the same corrosion conditions further support these findings, with the uniform phase separation in the glass becoming more pronounced with worsening base glass acid resistance.
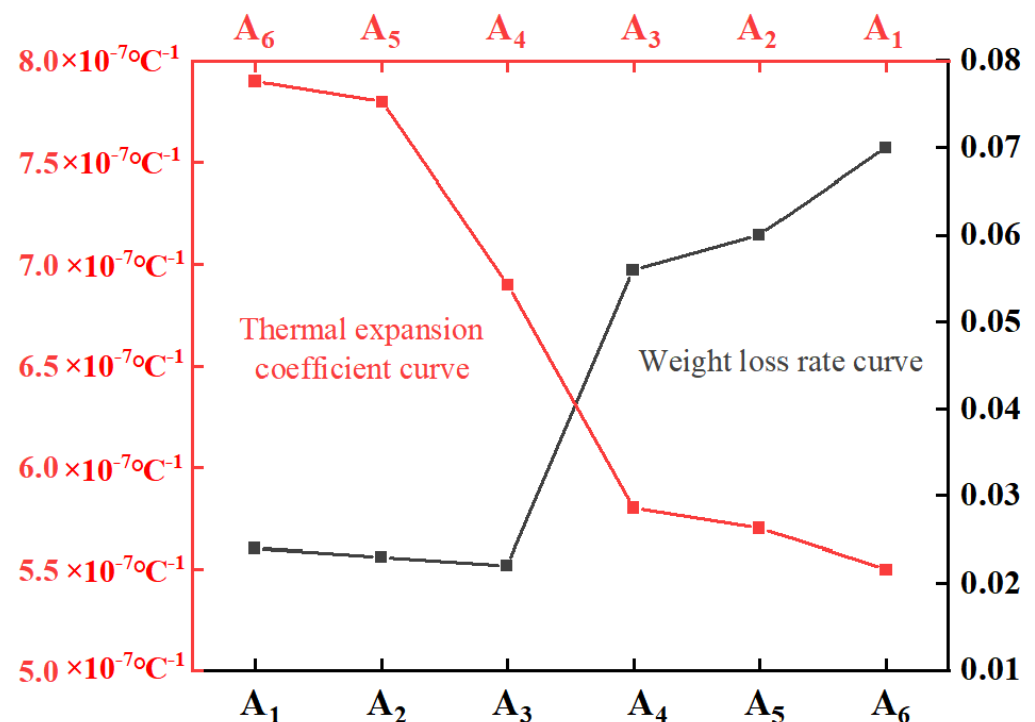


**Figure 8.** Basic glass expansion coefficient curve and acid resistance weight loss rate curve.

The data in Table 2 summarize the results obtained after performing calculations and fitting the Raman peaks of the six groups of basic borosilicate glass. The specific area percentage of each Qn component was determined from the $A_{1000}$ peak. The $I_p$ value of the glass phase was calculated using the provided formula, with the average number of non-bridging oxygen (NBO) atoms per tetrahedron, the average number of bridging angles per tetrahedron, and the glass transition temperature of each glass component also determined.

The data presented in Table 2 reveal that the isomorphic polyhedron (IP) values of the six sets of base glasses ($A_1$–$A_6$) and the number of bridged oxygen atoms within their tetrahedra are closely associated with the chemical stability of the base glass. A significantly lower degree of glass network polymerization was observed when the ratio of non-bridging oxygen (NBO) atoms to the sum of the NBO and bridged oxygen (BO) atoms lies in the 0.21–0.37 range, which implies that boron exists as $[BO_3]$ within the glass network structure at higher $B_2O_3$ contents, with a concomitant higher concentration of non-bridging oxygen atoms. This phenomenon is detrimental for reinforcing glass structures.

Furthermore, the glass transition temperature (Tg) was found to positively correlate with the basic oxide content of the base glass. Oxygen in borosilicate glasses can exist in two forms: bridging oxygen (BO) and non-bridging oxygen (NBO). The quantities of these two types of oxygen in each glass sample were determined by analyzing the peak areas obtained by Raman peak fitting, the results of which are summarized in Table 2. The information presented in Figure 8 and Table 2 reveals that increasing the $B_2O_3$ content gradually decreases the bridging oxygen content and progressively increases the non-

bridging oxygen content. The proportion of bridging oxygen in the glass is strongly associated with the $SiO_2$ content. The presence of sufficient free oxygen within the glass enables boron to exist in the network structure as $[BO_4]$ in instances where the alkaline oxide content is constant and the $B_2O_3$ content is low [24]. Consequently, the boron–oxygen tetrahedra form bonds with the silicon–oxygen tetrahedra and contribute to the formation of bridging oxygen (Si-O-B). However, the available free oxygen provided by the alkali metal oxide becomes insufficient when the $B_2O_3$ content surpasses a certain threshold, which limits the ability of boron to form boron–oxygen tetrahedra. As a result, boron is present within the glass network structure as $[BO_3]$, which increases the non-bridging oxygen content. This condition is unfavorable for strengthening the glass structure, as corroborated by microscopy.

As shown in Figure 9, Boron is retained within the glass network structure in the form of $[BO_3]$ and exhibits a layered arrangement in scenarios in which the available free oxygen provided by alkaline oxide is inadequate. However, B manifests as $[BO_4]$ within the borosilicate network when sufficient free oxygen is supplied from alkaline oxide; this transformation leads to a shift in the network structure of the glass from a layered configuration to a more compact framework, which enhances the chemical stability of the base glass as a consequence.
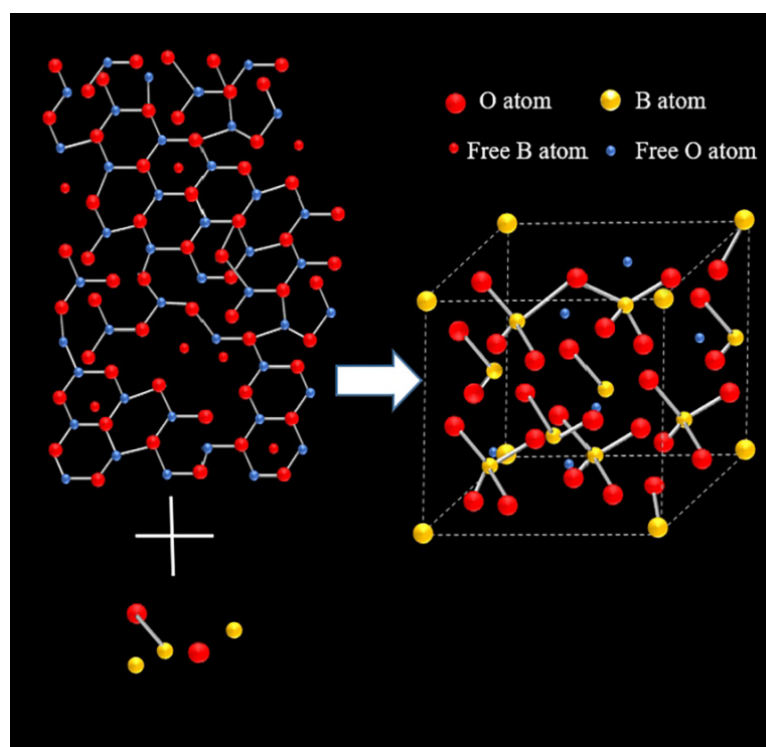


**Figure 9.** Network structure mechanism diagram of $B_2O_3$-reinforced borosilicate base glass.

As depicted in Figure 10, the vibrational peak observed at 765 cm$^{-1}$ corresponds to the Al-O stretching vibration of $AlO_4$, which is attributable to the presence of a small but constant quantity of $Al_2O_3$ in the system. Figure 7 shows that the intensity of the 765 cm$^{-1}$ vibrational peak of the borosilicate glass phase remains relatively unchanged with increasing $B_2O_3$ content. Typically, the vibrational peak at 990 cm$^{-1}$, which corresponds to the asymmetric Si-O-Si stretching vibration, is most prominent for a glass system. However, its position is slightly shifted and broadened owing to the coexistence of various bridging oxygen bonds in $Na_2O$-$B_2O_3$-$SiO_2$ low-expansion glasses. The peak near this position corresponds to a combination of $[BO_4]$ and $[BO_3]$ contributions.
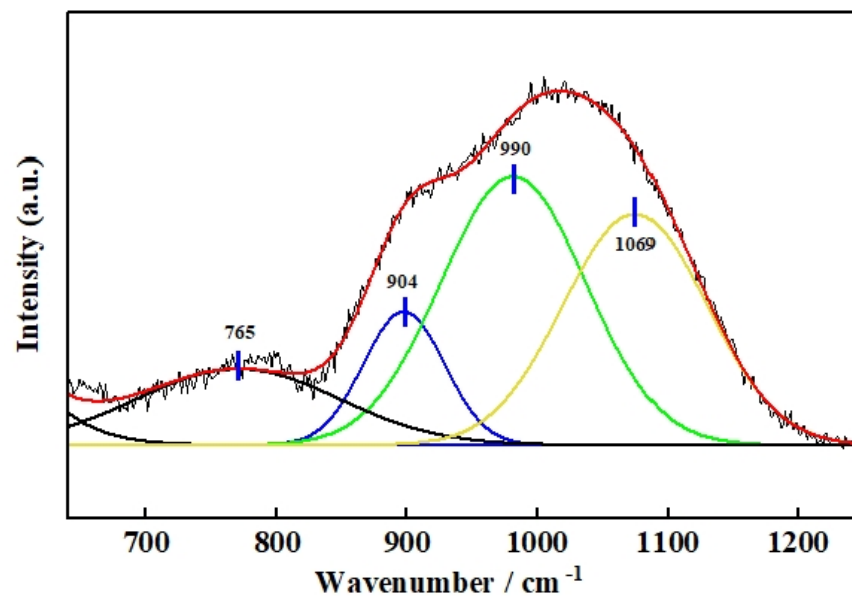
**Figure 10.** Raman spectrum at stretching vibration (700 cm$^{-1}$–1200 cm$^{-1}$) of A$_2$ base glass after peak separation and fitting.

In order to analyze in detail the shift and broadening of the glass stretching vibration peaks, for example, for A$_2$, the peak observed at 1069 cm$^{-1}$ corresponds to the B-O stretching vibration of glass [25], and its intensity increases with increasing B$_2$O$_3$ content. These results indicate that the amount of [BO$_3$] within the glass gradually increases because the available free oxygen provided by the alkali oxides is insufficient to combine with B$_2$O$_3$, thereby leading to the formation of [BO$_4$], which compromises the chemical stability of the glass as a consequence.

As shown in Figure 11, The Raman A$_{1000}$ data reveal that Q$_1$ and Q$_2$ do not noticeably fluctuate and show a relatively stable rise-and-fall pattern. The depolymerization of Q$_4$ to Q$_3$ in moving from A$_1$ to A$_6$ accelerates phase separation at higher temperatures, consistent with the scanning electron microscopy findings.
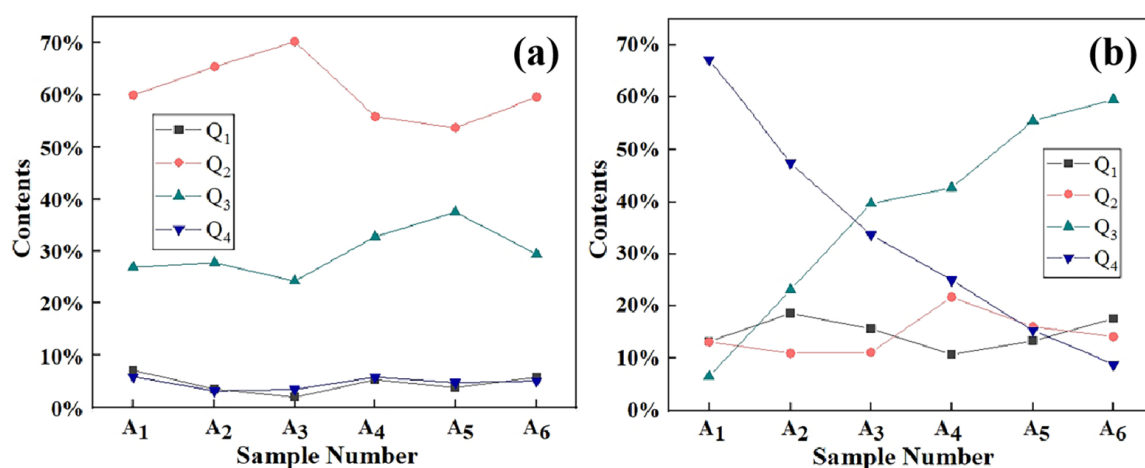


**Figure 11.** Percentage of Q$_n$ (n = 1,2,3,4) in bending vibration (**a**) and stretching vibration (**b**) of sample A$_1$–A$_6$.

## 4. Conclusions

(1) The microstructure and Raman spectra of the amorphous phase in borosilicate glass were investigated. It can be observed that the degree of phase separation in borosilicate

glass is closely related to the degree of polymerization (Ip) of the glass matrix. As the content of $B_2O_3$ increases from 12% to 15% and the content of mixed alkali oxides decreases from 7.5% to 6%, the Ip value of the glass matrix decreases from 3.82 to 1.98.

(2) With the increase in $B_2O_3$ content, when the free oxygen provided by alkali oxide is insufficient in the glass network, B exists in the glass network structure as [$BO_3$] with a layered structure. When the free oxygen provided by alkali oxide is sufficient, B exists in the borosilicate glass network structure in the form of [$BO_4$]. The change in the glass network structure makes the glass network more compact, and the chemical stability of the glass is better. When the $B_2O_3$ content is 15% and the mixed alkali oxide content is 6%, after immersing the glass in 38% sulfuric acid at a constant temperature of 85 °C for 200 h, the weight loss of the glass falls short of 0.03%.

(3) The Raman spectra revealed the bending and stretching vibrations of the glass network. The data of the fitted peaks show the cleavage of bridging oxygen bonds and the depolymerization of the glass network. In the base glass, the distribution of $Q_n$ shown by the Raman spectra demonstrates the structural phase separation effect of the glass network. Furthermore, the Raman depolymerization of the glass forms $Q_3$, promoting the occurrence of high-temperature phase separation, which was also confirmed by the SEM results.

## References

1. Munmun, A.; Singh, K.K.; Randhir, S. Hydrometallurgical recovery of manganese and nickel and isolation of tantalum from obsolete tantalum capacitor. *J. Environ. Chem. Eng.* **2022**, *10*, 108887.
2. Freeman, Y.; Lessner, P. Evolution of Polymer Tantalum Capacitors. *Appl. Sci.* **2021**, *11*, 5514. [CrossRef]
3. Susan, D.F.; Van Den Avyle, J.A.; Monroe, S.L.; Sorensen, N.R.; McKenzie, B.B.; Christensen, J.E.; Michael, J.R.; Walker, C.A. The Effects of Pre-Oxidation and Alloy Chemistry of Austenitic Stainless Steels on Glass/Metal Sealing. *Oxid. Met.* **2009**, *73*, 311–335. [CrossRef]
4. Yates, P.M.; Mallinson, C.F.; Mallinson, P.M.; Whiting, M.J.; Yeomans, J.A. An Investigation into the Nature of the Oxide Layer Formed on Kovar (Fe–29Ni–17Co) Wires Following Oxidation in Air at 700 and 800 °C. *Oxid. Met.* **2017**, *88*, 733–747. [CrossRef]
5. Donald, I.W.; Mallinson, P.M.; Metcalfe, B.L.; Gerrard, L.A.; Fernie, J.A. Recent developments in the preparation, characterization and applications of glass- and glass–ceramic-to-metal seals and coatings. *J. Mater. Sci.* **2011**, *46*, 1975–2000. [CrossRef]
6. Li, X.; Yazhenskikh, E.; Groß-Barsnick, S.M.; Baumann, S.; Behr, P.; Deibert, W.; Koppitz, T.; Müller, M.; Meulenberg, W.A.; Natour, G. Crystallization behavior of BaO–CaO–SiO$_2$–B$_2$O$_3$ glass sealant and adjusting its thermal properties for oxygen transport membrane joining application. *J. Eur. Ceram. Soc.* **2023**, *43*, 2541–2552. [CrossRef]
7. Salman, S.M.; Salama, S.N.; Abo-Mosallam, H.A. Crystallization characteristics and physico-chemical properties of glass–ceramics based on Li$_2$O–ZnO–SiO$_2$ system. *Boletín Soc. Española Cerámica Vidr.* **2017**, *56*, 205–214. [CrossRef]
8. Li, G.; Fu, R.; Agathopoulos, S.; Su, X.; He, Q.; Ji, Y.; Liu, X. Ultra-low thermal expansion coefficient of PZB/β-eucryptite composite glass for MEMS packaging. *Ceram. Int.* **2020**, *46*, 8385–8390. [CrossRef]
9. Dai, S.; Elisberg, B.; Calderone, J.; Lyon, N. Sealing glass-ceramics with near-linear thermal strain, part III: Stress modeling of strain and strain rate matched glass-ceramic to metal seals. *J. Am. Ceram. Soc.* **2017**, *100*, 3652–3661. [CrossRef]
10. Guo, M.; Jin, Y.; Zhang, R.; Yang, Z.; Peng, S. Low leakage rate of silicate glass modified with Al$_2$O$_3$ for solid oxide fuel cell. *J. Eur. Ceram. Soc.* **2022**, *42*, 3264–3270. [CrossRef]
11. Madheshiya, A.; Singh, A.K.; Shweta; Mishra, R.K.; Dey, K.K.; Ghosh, M.; Srivastava, K.K.; Garg, P.; Gautam, C. Synthesis, physical, optical and structural properties of SrTiO$_3$ borosilicate glasses with addition of CrO$_3$. *Bull. Mater. Sci.* **2023**, *46*, 34. [CrossRef]

12. Singh, K.; Walia, T. Review on silicate and borosilicate-based glass sealants and their interaction with components of solid oxide fuel cell. *Int. J. Energy Res.* **2021**, *45*, 20559–20582. [CrossRef]
13. Wan, J.; Cheng, J.; Lu, P. Effect of $Al_3O_3$ on the thermal expansion and phase separation of borosilicate glass. *J. Chin. Ceram. Soc.* **2008**, *36*, 544.
14. Hordieiev, Y.S.; Zaichuk, A.V. Study of the Influence of $R_2O_3$ (R = Al, La, Y) on the Structure, Thermal and some Physical Properties of Magnesium Borosilicate Glasses. *J. Inorg. Organomet. Polym. Mater.* **2023**, *33*, 591–598. [CrossRef]
15. He, F.; Fang, Y.; Liu, J.; Cheng, J.S. Effect of $B_2O_3$ on structure and properties of borosilicate glass. *J. Wuhan Univ. Technol.* **2012**, *34*, 1–4.
16. Bengtsson, F.; Pehlivan, I.B.; Österlund, L.; Karlsson, S. Alkali ion diffusion and structure of chemically strengthened $TiO_2$ doped soda-lime silicate glass. *J. Non-Cryst. Solids* **2022**, *586*, 121564. [CrossRef]
17. Gu, Q.B.; Ni, J.M. Preparation and Analysis of Doped $TiO_2$ in the $Bi_2O_3$-$SiO_2$-$ZnO$-$B_2O_3$ Low-Melting Sealing Glasses. *Key Eng. Mater.* **2012**, *509*, 308–313. [CrossRef]
18. Chen, Y.; Yang, S.; Wang, Q.; He, S. Effect of (BaO + CaO)/$Al_2O_3$ ratio (1.7~2.0) on the structure and Al-Li association of $BaO$-$CaO$-$Al_2O_3$-$CaF_2$-$Li_2O$ mold flux. *J. Non-Cryst. Solids* **2022**, *584*, 121522. [CrossRef]
19. Chung, S.-Y.; Kim, Y.-M.; Kim, J.-G.; Kim, Y.-J. Multiphase transformation and Ostwald's rule of stages during crystallization of a metal phosphate. *Nat. Phys.* **2008**, *5*, 68–73. [CrossRef]
20. Colomban, P.; Tournie, A.; Bellot-Gurlet, L. Raman identification of glassy silicates used in ceramics, glass and jewellery: A tentative differentiation guide. *J. Raman Spectrosc.* **2006**, *37*, 841–852. [CrossRef]
21. Deng, L.; Zhang, X.; Zhang, M.; Jia, X.; Zhang, Z.; Li, B. Structure and properties of in situ synthesized $FeSi_2$-diopside glass ceramic composites from Bayan Obo tailings, blast furnace slag, and fly ash. *J. Alloys Compd.* **2019**, *785*, 932–943. [CrossRef]
22. Zhang, M.-X.; Kelly, P.M. Crystallographic features of phase transformations in solids. *Prog. Mater. Sci.* **2009**, *54*, 1101–1170. [CrossRef]
23. Zhang, Y.; Li, H.; Liu, S.; Wu, N.; OuYang, S. Raman spectroscopic study of irregular network in the process of glass conversion to $CaO$-$MgO$-$Al_2O_3$-$SiO_2$ glass-ceramics. *J. Non-Cryst. Solids* **2021**, *563*, 120701. [CrossRef]
24. Santos, A.G.; Moulton, B.J.; Cabral, A.A. Discoveries about the structure of alkaline earth-bearing borosilicate glasses doped with $TiO_2$ revealed by Raman spectroscopy. *J. Non-Cryst. Solids* **2022**, *578*, 121349. [CrossRef]
25. Kaur, M.; Singh, S.P.; Mudahar, D.S.; Mudahar, G.S. Structural investigation of $B_2O_3$-$Li_2CO_3$-$Al_2O_3$ glasses by molar volume measurements and FTIR spectroscopy. *Mater. Phys. Mech.* **2012**, *15*, 66–73.